HAL
open science

Chemical Passivation with Phosphonic Acid Derivatives of ZnO Deposited by Atomic Layer Deposition and Its Influence on the Halide Perovskite Interface

Olivier Fournier, Claire Darin Bapaume, Davina Messou, Muriel Bouttemy, Philip Schulz, François Ozanam, Laurent Lombez, Nathanaelle Schneider, Jean Rousset

To cite this version:

Olivier Fournier, Claire Darin Bapaume, Davina Messou, Muriel Bouttemy, Philip Schulz, et al.. Chemical Passivation with Phosphonic Acid Derivatives of ZnO Deposited by Atomic Layer Deposition and Its Influence on the Halide Perovskite Interface. ACS Applied Energy Materials, 2021, 10.1021/acsaem.1c00612 . hal-03254303

HAL Id: hal-03254303

https://hal.science/hal-03254303

Submitted on 1 Dec 2021

HAL is a multi-disciplinary open access archive for the deposit and dissemination of scientific research documents, whether they are published or not. The documents may come from teaching and research institutions in France or abroad, or from public or private research centers.

L'archive ouverte pluridisciplinaire **HAL**, est destinée au dépôt et à la diffusion de documents scientifiques de niveau recherche, publiés ou non, émanant des établissements d'enseignement et de recherche français ou étrangers, des laboratoires publics ou privés.

Chemical passivation with phosphonic acid derivatives of ZnO deposited by atomic layer deposition and its influence on halide perovskite interface

Olivier Fournier[1,2,*], Claire Darin Bapaume[2,3], Davina Messou[2,4], Muriel Bouttemy[2,4], Philip Schulz[2,3], François Ozanam[5], Laurent Lombez[2,3], Nathanaelle Schneider[2,3], Jean Rousset[1,2]

[1] EDF R&D, IPVF, 18 boulevard Thomas Gobert, 91120 Palaiseau, France

[2] Institut Photovoltaïque d'Ile-de-France (IPVF), 18 boulevard Thomas Gobert, 91120 Palaiseau, France

[3] CNRS, UMR 9006, Institut Photovoltaïque d'Ile-de-France (IPVF), 18 boulevard Thomas Gobert, 91120 Palaiseau, France

[4] Institut Lavoisier de Versailles (ILV), Université de Versailles Saint-Quentin en Yvelines, Université Paris-Saclay, CNRS, UMR 8180, 45 avenue des Etats-Unis, 78035 Versailles Cedex, France

[5] PMC, CNRS, Ecole Polytechnique, IP Paris, 91128 Palaiseau, France

Abstract: We report on the modification of zinc oxide thin films deposited by atomic layer deposition (ALD-ZnO) with various phosphonic acid derivatives. Particularly, three molecules differing by their spacer and functionalizing groups were tested: 2-aminoethylphosphonic acid (2-AEPA), 4-aminobenzylphosphonic acid (4-ABzPA) and 4-fluorobenzylphosphonic acid (4-FBzPA). The resulting surfaces were investigated with surface sensitive characterization techniques such as X-ray photoelectron spectroscopy and attenuated total reflection IR spectroscopy. We find differences in the phosphonic acid film growth, mostly driven by the nature of the functionalizing group: the amine-based molecules tend to cover the surface with disordered layers or multilayers whereas the 4-FBzPA layer rather exhibits features of a monolayer. Finally, 2-AEPA and 4-FBzPA have been used as a mean to passivate the reactive interface between ALD-ZnO and a hybrid organic inorganic metal halide perovskite. Morphological and structural studies were carried out with scanning electron microscopy and X-ray diffraction and solar cells using these layers as electron transport layers were synthetized. With a highest power conversion efficiency of 4.1%, the direct application of these surface modifications into complete devices is shown not to be enough to achieve high-efficiency solar cells with ALD-ZnO.

INTRODUCTION

Zinc oxide (ZnO) is an extensively studied n-type semiconductor, with very versatile applications due to its expedient optoelectronic properties such as a wide bandgap (3.3 eV)[1], a large carrier mobility (~ 100 $cm^2 V^{-1} s^{-1}$)[2] or its variety of potential dopants (Al, Ti, Ga, B, F, N, ...)[3] suitable for instance in UV-light emitting devices (LED), thin film transistors, detection of chemicals[4–6] or solar cells, where it is used in many technologies such as copper indium gallium selenide (CIGS)[7], organic[8] or perovskite solar cells.[9,10] It is a well-known transparent conductive oxide composed of abundant and non-toxic elements which can be synthetized by various thin-film deposition methods into different shapes and morphologies (nanostructures, thin films, single crystals ...).[6,11]

For perovskite solar cells the improvement of device performance, and particularly stability, is closely linked to chemical passivation at the interfaces.[12,13] ZnO/halide perovskite interfaces are generally prone to suffer from a strong thermal instability[14], which can be mitigated by the introduction of molecular interlayers.[15] Different strategies have been employed to reach good efficiencies in n-i-p configurations (*i.e.* absorber deposited on top of the electron transport layer): treating the surface with self-assembled monolayers[16,17], chlorinated compounds[18], WO_3[19], ethanedithiol[20], MgO/ethanolamine[21], ZnS[22],

Table 1: Summary of the experimental conditions for the grafting of the different samples used in this study.

Sample	Substrate	Molecule	Immersion time	Concentration	Superstrate
ZnO-ref	Si / ZnO	-	10 min	-	-
ZnO-AEPA	Si / ZnO	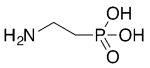	10 min	1 mM	-
ZnO-ABzPA	Si / ZnO	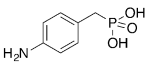	10 min	1 mM	-
ZnO-FBzPA	Si / ZnO	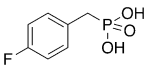	10 min	1 mM	-
Ref-pvk	FTO / ZnO	-	10 min	1 mM	$(MA,FA,Cs)Pb(I,Br)_3$
AEPA-pvk	FTO / ZnO	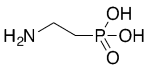	10 min	1 mM	$(MA,FA,Cs)Pb(I,Br)_3$
FBzPA-pvk	FTO / ZnO	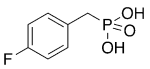	10 min	1 mM	$(MA,FA,Cs)Pb(I,Br)_3$

Al-doping[23], reducing the perovskite annealing temperature [24] or changing the perovskite absorber composition[25]. Atomic layer deposition (ALD) can be used for the deposition of conformal and dense ZnO layers, and previous reviews have reported its application in perovskite solar cells[26–28]. The applications of ALD-ZnO mostly concern p-i-n configurations where the oxide is deposited on top of the perovskite; still, the use of ALD-ZnO as ETL in n-i-p structure is relatively rare[29].

Functionalization through molecular grafting of zinc oxide has been extensively studied in the literature, whether on ZnO nanostructures[30–32] or films[33,34]. Grafted molecules of all shapes and sizes can be designed depending on the purpose of the grafting, from large fullerene-derivatives[35] to smaller molecules with only a few carbon atoms[33]. A typical architecture for such molecules consists in an anchoring group, a spacer and a tail group. The spacer influences the organization of the layer (π-π interactions between aryl rings, van der Walls interactions between alkyl chains) as well as its conductivity (conjugated *vs.* unconjugated systems[36]). The tail group defines the functionality of the final film, which can change its wettability, its optoelectronic properties[33,37], serve as a catalyst for further reactions[5,38] or even passivate defects at the interface to adjacent layers[39].

Different chemical groups have been used as anchors on ZnO including silanes, thiols, carboxylic acids and phosphonic acids. Silanes have proven to be able to form bonds with ZnO but are limited by the strict control over the experimental conditions they require, especially in regard of the amount of water during the process which promotes homocondensation of the molecules[40]. Carboxylic groups have also been used to some extent but result in only weakly grafted layers[41]. The relative strength of the bond of thiol and phosphonic acids with the metal has been investigated by Perkins *et al.*[42] by comparing the grafted layer obtained with 1-hexanethiol and 1-hexanephosphonic acid on similar substrates. The authors claim that phosphonic acid is a better linking group than thiol, showing especially better thermal stability. Phosphonic acids are thus a key anchoring group for grafting on several oxides (including also TiO_2[43], ZrO_2[44] or Al_2O_3[45]) and have, as such, been subject of dedicated studies to determine the grafting chemical process[46]. The process involves an acid-base condensation mechanism between one (or more) hydroxyl groups of the metal oxide surface and the phosphonic acid, which leads to different binding configurations referred to as mono-, bi- or tridentate depending on the number of -OH groups involved.

We chose to investigate three different molecules: 2-aminoethylphosphonic acid (2-AEPA), 4-aminobenzylphosphonic acid (4-ABzPA) and 4-fluorobenzylphosphonic acid (4-FBzPA). Hence, linear unconjugated (2-AEPA) and aromatic conjugated (4-ABzPA and 4-FBzPA) systems are compared as well as different chemical functional groups. The amine termination can, for instance, be used to initiate further reactions on the surface of the modified substrate, while the fluorine functionalization rather aims at making the surface more hydrophobic. In the case of 4-ABzPA and 4-FBzPA, the change in the functional group can

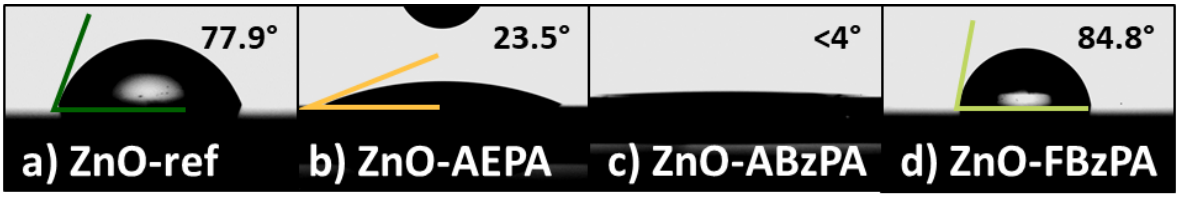

Figure 1: Static contact angles of deionized water on a) ZnO-ref, b) ZnO-AEPA, c) ZnO-ABzPA and d) ZnO-FBzPA, after 10 min immersion. The values are given as an average over different samples.

also greatly influence the energetics of the surface due to the change in dipole moment of the molecule, as achieved in OSCs.[8,33] 4-ABzPA has also been used to initiate the polymerization of polyaniline films on indium-tin oxide (ITO) substrate,[47] or as a linker between a metal oxide scaffold and CdSe quantum dots for photocathodes[48] while 2-AEPA has mostly been reported as reaction auxiliary. Due to its high molecular dipole moment, 4-FBzPA can easily modify the work function of ITO substrates in organic LEDs.[49] Its grafting process on ZnO has been specifically assessed by density functional theory (DFT) calculations[50], which describe a tridentate binding mode.

In the present work, we aim at grafting 4-FBzPA, 4-ABzPA and 2-AEPA on top of ZnO deposited by atomic layer deposition (ALD) on silicon wafers or fluorine-doped tin oxide (FTO), and assessing whether the change in the architecture of the grafted molecules (spacer, tail group) influences the grafting. The modification of the substrate is probed with surface-sensitive characterization techniques: contact angle measurements, Fourier transform infrared spectroscopy (FTIR) and X-ray photoemission spectroscopy (XPS). In order to investigate the effect of the grafting as chemical passivation, we chose to study how the interface between ZnO and triple cation lead mixed-halide perovskite is affected by the grafting of 2-AEPA and 4-FBzPA, and how this translates in terms of cell performances.

RESULTS

Characterization of the modified zinc oxide layer. First, the modification of a 50 nm-thick ZnO layer deposited by ALD with 2-AEPA, 4-ABzPA and 4-FBzPA was characterized. Surface-sensitive techniques were used to analyze the surface of ZnO substrates immersed in different solutions of phosphonic acid derivatives – thereafter mentioned as "ZnO-X" (with X = AEPA, ABzPA or FBzPA) – and control ZnO substrates immersed in the sole solvent – thereafter mentioned as "ZnO-ref". The use of ALD implies that the roughness of the ZnO layer will follow that of the underlying substrate.[51] Si substrates have been chosen in order to provide a flat surface more suitable for angle resolved-XPS (AR-XPS) and FTIR analysis. A short description of the samples used throughout this study is presented in Table 1.

Contact angle measurements. Contact angle measurements have been performed in order to assess a change in the nature of the ZnO surface, through a modification of its wettability, induced by the presence of grafted molecules.

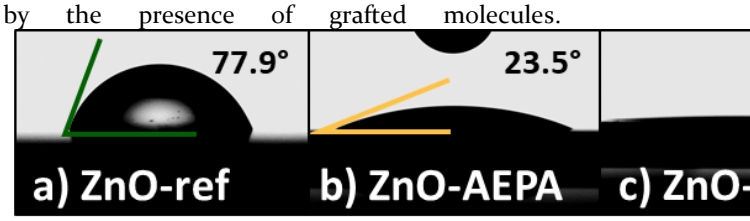

Figure 1 presents the static contact angle between the samples immersed for 10 min and deionized water for a molecule concentration of 1 mM (2-AEPA, 4-ABzPA or 4-FBzPA) and for the reference sample. The static contact angle measured for ZnO-ref is 77.9 ± 1.4°. This angle varies upon modifying the surface. ZnO-FBzPA tends to have a more hydrophobic surface (84.8 ± 0.7°) in agreement with a fluorine termination, while amine-based samples (ZnO-AEPA and ZnO-ABzPA) yield more hydrophilic surfaces (23.5 ± 1.6° and <4° respectively). These results indicate an effective modification of the ZnO surface. The integrity of the ZnO film after immersion was probed by scanning electron microscopy (SEM), and grazing incidence X-ray diffraction (GI-XRD). In the case of ZnO-ref in EtOH:H_2O, a degradation of the ZnO layer appears clearly after a long immersion time (24 h), as seen in the diffractograms (Figure S1) and micrographs (Figure S2). This degradation is mitigated when the phosphonic acid molecules are added to the solution, which implies that a protective layer is grafted on top of the ZnO film.

XPS. XPS has been used to confirm the molecular grafting on ZnO substrate along with the chemical evolution at the surfaces (~ 10 nm depth probed). The survey spectra of the three modified samples (Figure S3) clearly evidence the presence of molecules at the surface with the detection of P and N (2-AEPA and 4-ABzPA) or F (4-FBzPA) elements depending on the different groups' assembly. Zn, O and C elements are also visible and related to the substrate, the adventitious carbon contamination, and the alkyl chain or aromatic group. The corresponding high energy resolution spectra of the main core levels Zn $2p_{3/2}$, O 1s, P 2p, F 1s and

N 1s are presented in Figure 2 to accurately assess chemical environments (C 1s is presented in Figure S4). ZnO-ref is considered first to determine the initial spectral signature of the substrate. Zn $2P_{3/2}$ peak is decomposed using two contributions at binding energies (BE) of 1022.3 eV (Zn_a) and 1023.2 eV (Zn_b) as already reported for

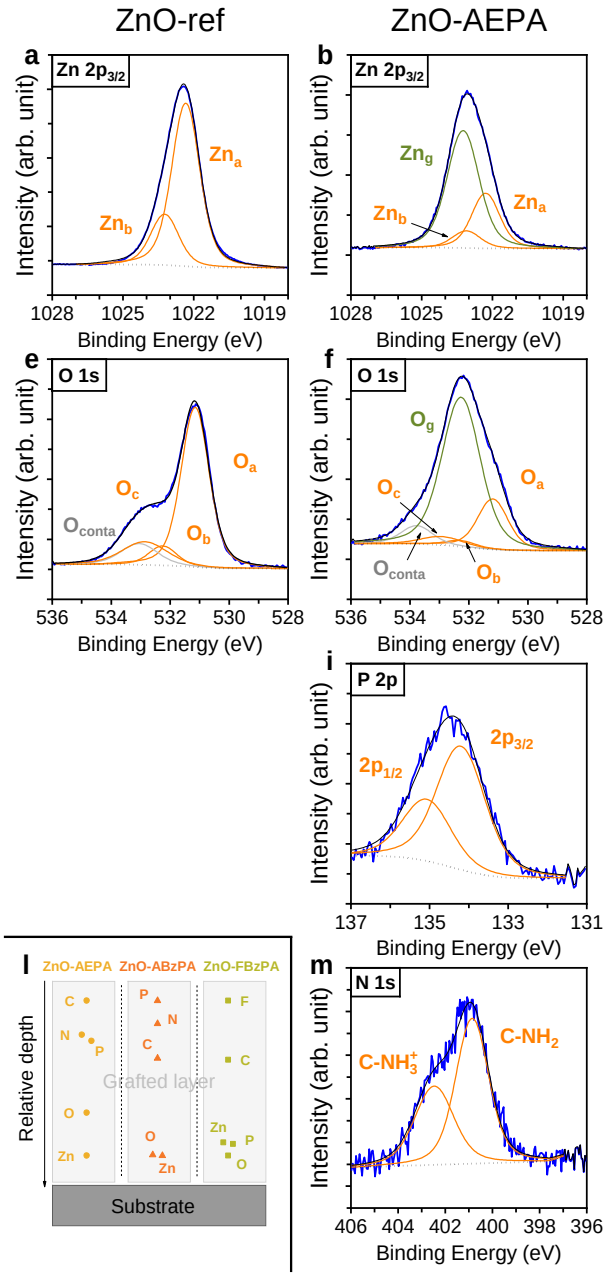

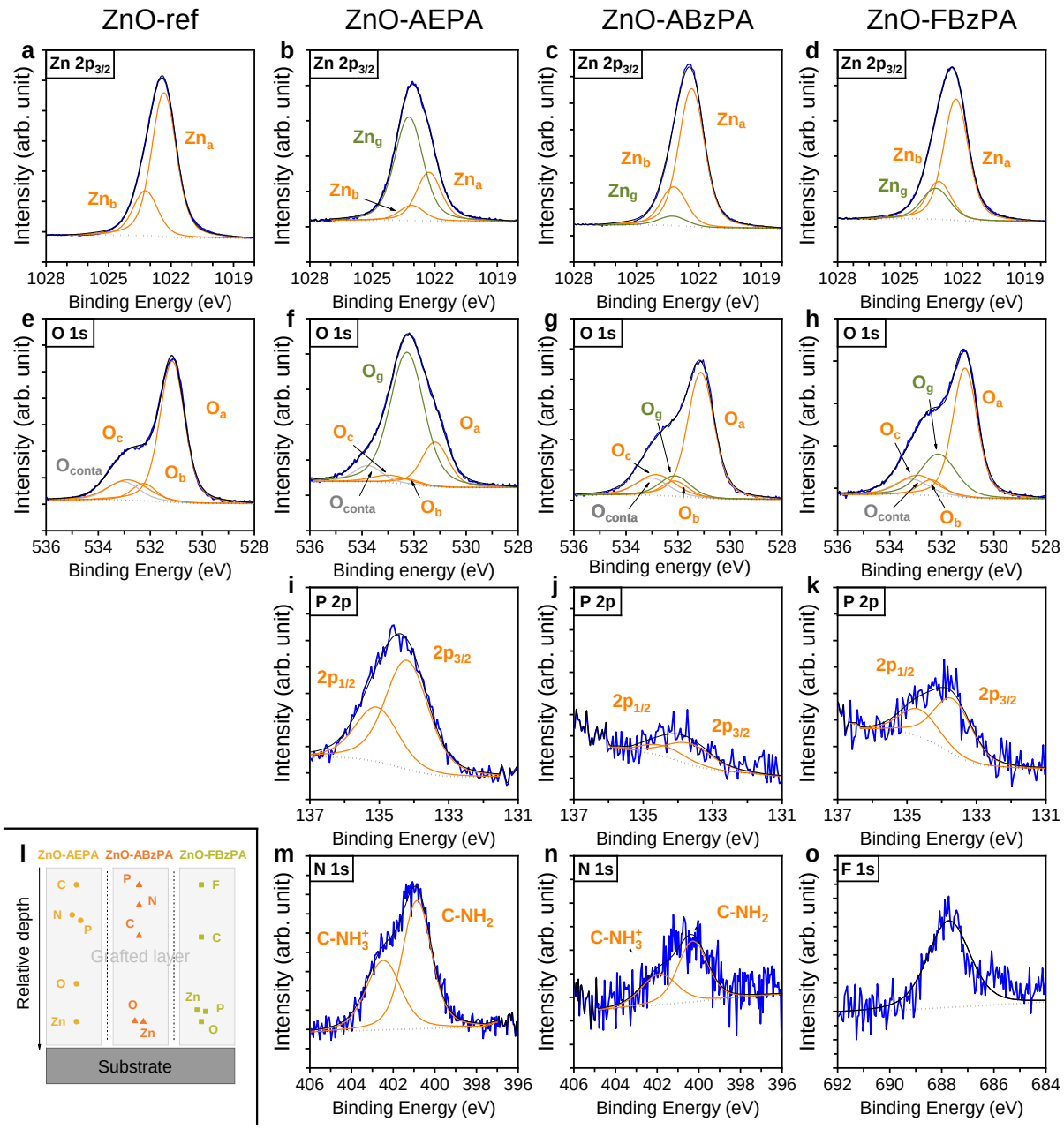

Figure 2: Summary of XPS measurements made at 0° incidence angle on reference ZnO (first column) and modified ZnO with 1 mM 2-AEPA (second column), 4-ABzPA (third column) and 4-FBzPA (fourth column). High resolution spectra of a)-d) Zn $2p_{3/2}$, e)-h) O 1s, i)-k) P 2p, m), n) N 1s and o) F 1s. l) Relative depth plot of the relevant chemicals as extracted from angle-resolved XPS. For all high resolution spectra, experimental data are in plain blue, fitted data in plain dark and background in dotted black.

bulk ZnO[52,53]. The O 1s peak requires four contributions, the one at 531.1 eV being assigned to Zn-O bulk network (O_a/Zn_a), the other at 532.3 eV and 532.8 eV to Zn-O surface networks (O_b and O_c/Zn_b) due to adsorbed O or water and presence of (oxy)-hydroxide species and the last at 533.1 eV to O involved in the carbonaceous contamination (O_{conta}).[35,36] For all modified samples, these features are still present but with a change in their relative proportion and the appearance of new contributions, also for C 1s. This indicates that the ZnO lattice (O_a/Zn_a) is still detected and the coverage uncomplete (O_b and O_c/Zn_b surface contributions not totally canceled). Their intensities vary with the molecular grafting acting as an attenuation filter for the photoelectron emitted beneath with respect to the nature of the molecules, their intimate organization during grafting and the coverage rate. Note that as for C contamination[54], the screening effect must differ with the kinetic energy of the photoelectrons, i.e. attenuation is not the same for all the photopeaks considered. Consequently, the surface contributions intensity are exacerbated and

Table 2: Vibration modes position extracted from the different FTIR spectra of ZnO-AEPA, ZnO-ABzPA and ZnO-FBzPA.

Vibration mode	ZnO-AEPA (cm-1)	ZnO-ABzPA (cm-1)	ZnO-FBzPA (cm-1)
P-O modes	950-1200	950-1200	950-1200
ν (C-F)			1230 (aromatic)
δ (CH_2)	1468	1468	1485
ν (C=C)		1515 (disubs. benzyl)	1515 (disubs. benzyl)
δ (NH_3^+)	1520		
δ (NH_2)	1630		

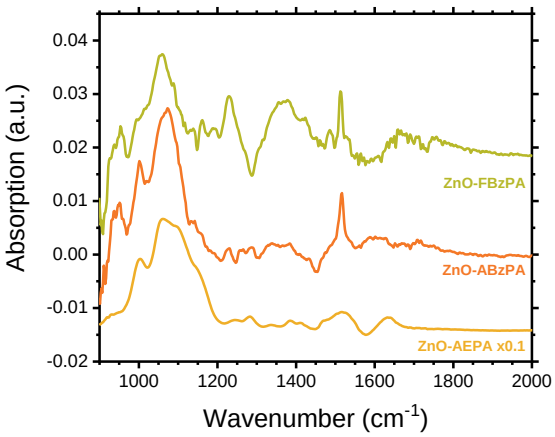

Figure 3: ATR-FTIR spectra of ZnO-AEPA, ZnO-ABzPA and ZnO-FBzPA. The Si-ZnO substrates were taken as reference. Note that absorption of ZnO-AEPA is multiplied by 0.1.

quantification not straightforward (determination of the attenuation coefficient required). The appearance of the new Zn contribution Zn_g (1023.3 eV) is concomitant with a common increase of O_g contribution, associated to the new surface environment after grafting, and consistent with the previous consideration about the restriction of the depth probed. Thus, this trend is more pronounced on the ZnO-AEPA sample presenting the highest molecular grafting rate (Zn/P = 1.1 vs 38.2 and 11.0 for ABzPA and FBzPA respectively). Specific contributions associated to the molecules (2-AEPA, 4-ABzPA, 4-FBzPA) are identified on the O and C spectra (

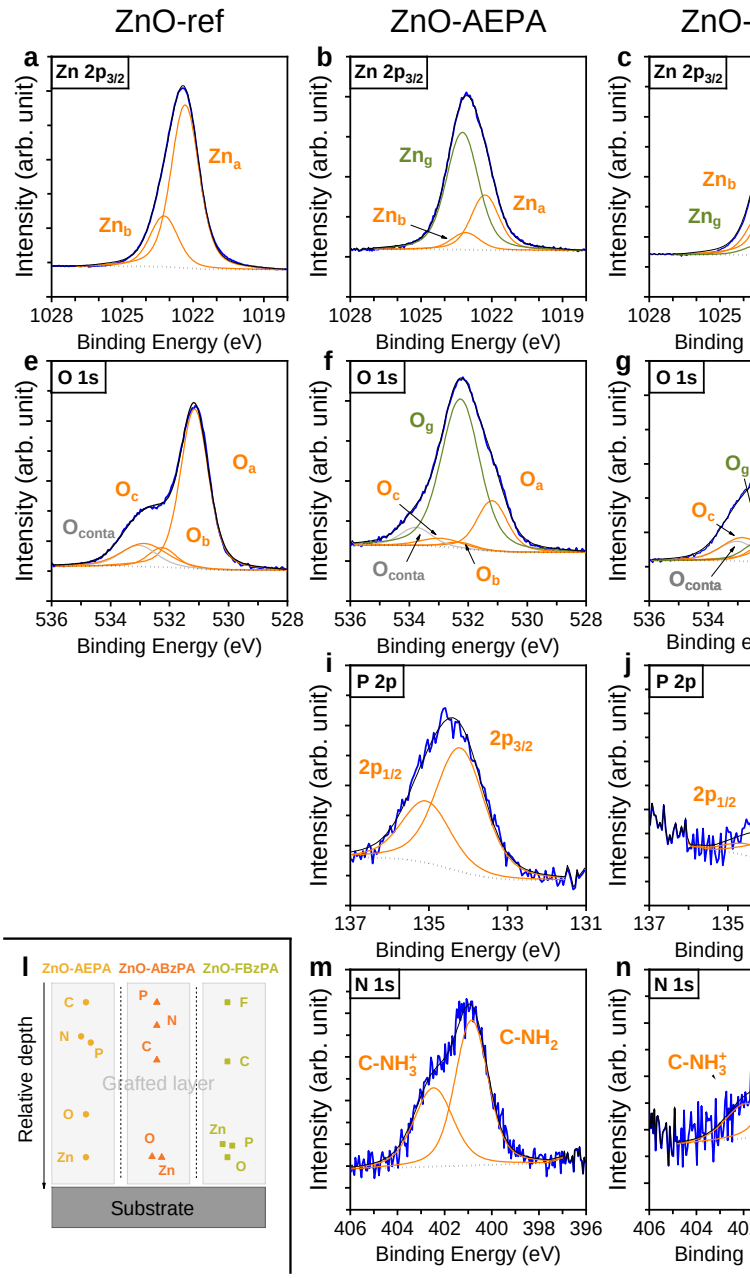

Figure 2 and S4). Note that on the C spectra, the Π-Π* satellite attesting for the aromatic cycle presence is not evidenced as it overlaps the C_{conta}

contribution. A unique environment is considered for P in the phosphonic group (one spin-orbit doublet). This is the same for F 1s whereas two contributions are required for the fitting of N peak and assigned to NH_2, NH_3^+ environments[47]. BE values are reported in SI (Table S1) and will be discussed later on.

The grafting anchoring site and molecules organization have been investigated using AR-XPS. The average vertical distribution of each element, Zn, O, C, P, N and F is presented in a relative depth plot (

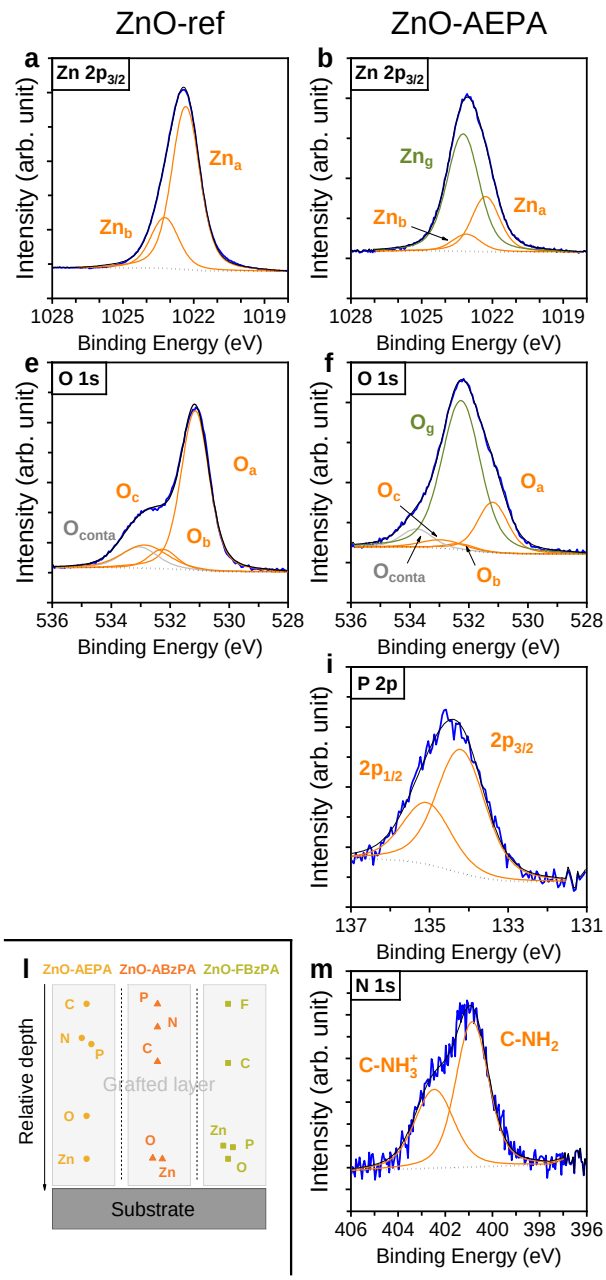

Figure 2.h). This plot is based on the comparative evolution of the areas ratio of the different elements measured at each considered detection angle. It enables to display a relative order of appearance/disappearance of the elements across the layer. In any case, the constitutive elements of the substrate Zn and O are located deeper, as expected. Regarding ZnO-AEPA and ZnO-ABzPA, there is no clear order in the spatial organization of the grafted molecules (C, P and N), whereas for ZnO-FBzPA, a main orientation is shown, with P oriented toward ZnO surface and F to the outside.

ATR. The structure of the modified layer was also analyzed using attenuated total reflection infrared spectroscopy (ATR-FTIR). For that purpose, the Si substrate is shaped as multiple-internal-reflection element in order to increase the signal-to-noise ratio from the thin grafted layer deposited on this substrate. For each molecule, a reference spectrum was acquired on a Si/ZnO substrate which was subsequently modified with the desired molecule. The sample was then mounted back at the same spatial location on the sample holder, so that the resulting absorbance spectrum computed after recording of the IR spectrum on the modified sample is characteristic of the changes induced by the grafting process. Figure 3 presents the ATR-FTIR spectrum of the modified layers in the fingerprint region (below 2000 cm^{-1}). The relevant identified peak positions are listed in Table 2. For all the molecules, the presence of the bands related to phosphonic species in the 950-1200 cm^{-1} range[55] attests the presence of the molecules at the surface of the film, and their grafting since the spectra from the surface molecule significantly differ from that of the free molecules. In ZnO-AEPA, the amine functional group can be associated with the two broad absorption bands at 1630 cm^{-1} and 1520 cm^{-1} (the former is ascribed to the NH_2 in-plane bending

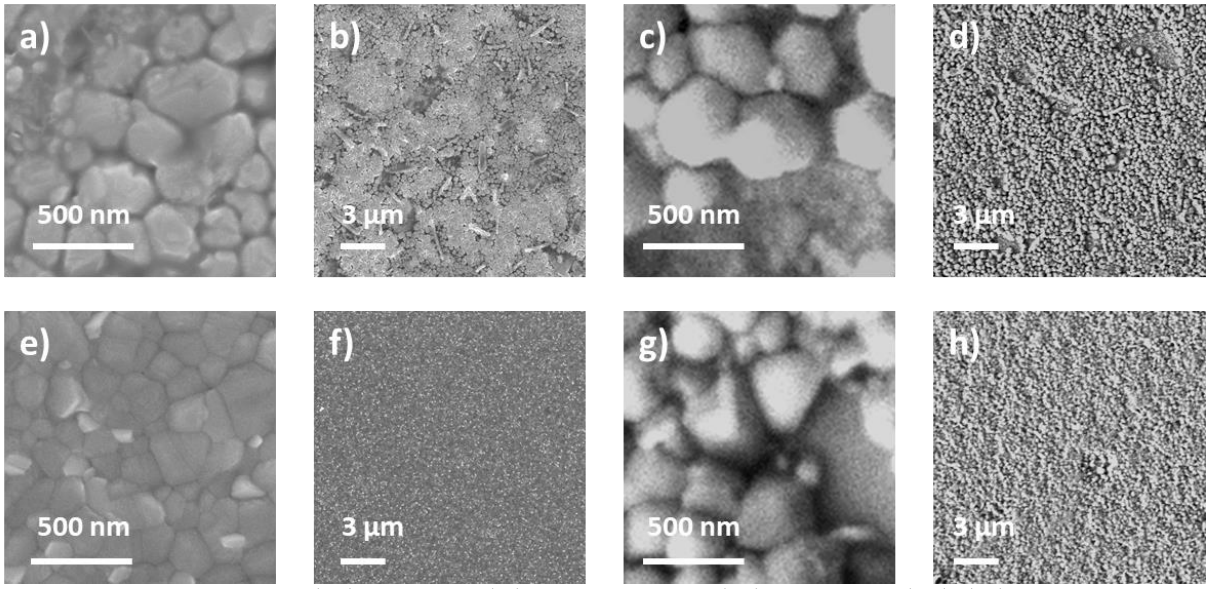

Figure 4: SEM micrographs of a)-d) Ref-pvk, of e)-f) AEPA-pvk and of g)-h) FBzPA-pvk. b), d), f),h) Low magnification surface micrographs. a), c),e),g) High magnification surface micrographs. The perovskite surface in the case of Ref-pvk and FBzPA-pvk is inhomogeneous and damaged.

modes of primary amines, the latter to the unresolved symmetric and asymmetric bending modes of protonated amines[56]). The latter peak has a shoulder at 1468 cm^{-1} ascribed to the methylene bending mode, which can also be found on ZnO-FBzPA. The two aromatic molecules (ZnO-ABzPA and ZnO-FBzPA) feature an intense peak at 1515 cm^{-1} characteristic of a substituent-sensitive aromatic-ring mode in di-substituted benzyl[57]. Another sharp intense peak in ZnO-FBzPA at 1230 cm^{-1} can be attributed to an aryl-F stretching mode[57].

Analysis of the ZnO/perovskite interface. Modifying the chemical state of a surface can lead to significant changes in the interfacial chemistry. Here, we were interested in probing the effect of the grafting of 2-AEPA and 4-FBzPA on the interface between ZnO substrate and hybrid perovskite, which have been widely used in solar cells. The grafting of 4-ABzPA was also considered but lead to non-working devices. A design that corresponds to a conventional n-i-p perovskite solar cell structure was chosen (as described in Hadouchi *et al.*[9]). Hence the substrate consists in commercial FTO-coated glass, covered with 15 nm ZnO deposited by ALD. The substrates are modified with 1 mM 2-AEPA or 4-FBzPA for 10 minutes in EtOH:H_2O (19:1), and a triple cation perovskite (solution composition $Cs_{0.05}(FA_{0.83}MA_{0.17})_{0.95}Pb(I_{0.83}Br_{0.17})_3$, MA = $CH_3NH_3^+$ methylammonium, FA = $CH(NH_2)_2^+$ formamidinium) is deposited on top. The sample with perovskite deposited on ZnO-AEPA (resp. ZnO-FBzPA and ZnO-ref) is referred to as AEPA-pvk (resp. FBzPA-pvk and Ref-pvk, cf. Table 1). The morphology of the perovskite films was analyzed by SEM.

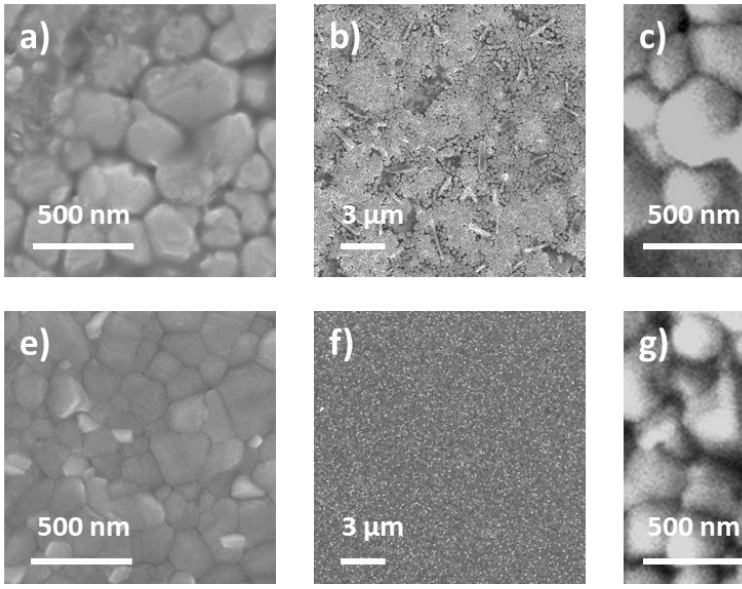

Figure 4 presents micrographs of the surface of the perovskite layer of Ref-pvk, FBzPA-pvk and AEPA-pvk at different magnifications. Additional images including cross sections are available in supplementary information. From the surface images, the morphology of the perovskite appears highly dependent on the modification of ZnO by the molecules. The perovskite of AEPA-pvk forms similarly to what has been reported in working cells[58]. On the other hand, the perovskite films of Ref-pvk and FBzPA-pvk show a dendritic crystallization or do not completely cover the substrate, which evidences a deteriorated film formation. On cross-sectional images, a pronounced formation of cavities between the grains can be observed for Ref-pvk compared to AEPA-pvk. Furthermore, the ZnO layer forms a clear continuous layer in AEPA-pvk (figure S9.b),

while it is hardly the case in Ref-pvk (figure S9.a). This could suggest a degradation of the ZnO layer due to the perovskite deposition in the case of Ref-pvk.

These very different morphological features between Ref-pvk and AEPA-pvk have been further explored with a structural characterization carried out by XRD. The corresponding diffractograms are shown in Figure S5. In both cases, the film crystallizes into the photo-active perovskite phase as confirmed by the high intensity diffraction peaks at 2θ = 14.0°, 19.9° and 24.4°, characteristic of the $Cs_{0.05}(FA_{0.83}MA_{0.17})_{0.95}Pb(I_{0.83}Br_{0.17})_3$ perovskite crystal structure[59] (full indexation available in SI). In Ref-pvk additional peaks appear at 2θ = 12.6°, 38.7° and 39.5°. These peaks are characteristic of lead iodide PbI_2 which originates from the degradation of the perovskite[60]. The presence of lead iodide has also been confirmed by UV-Vis

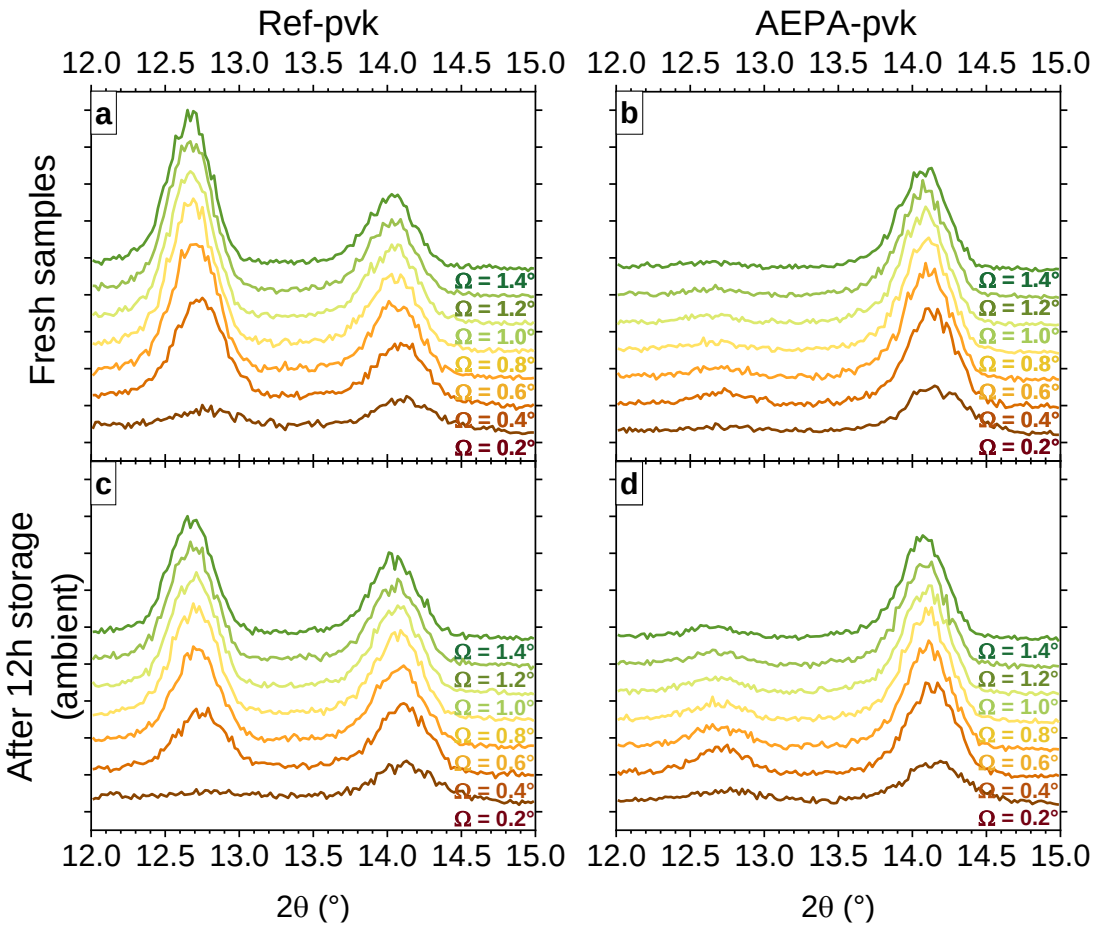

Figure 5: GI-XRD diffractograms with varying grazing incidence angles from **Ω** = 0.2° to 1.4° of a) fresh Ref-pvk, b) fresh AEPA-pvk, c) stored Ref-pvk and d) stored AEPA-pvk. The samples were stored on a shelf in ambient atmosphere and exposed to light. The region of interest focuses on the main PbI_2 peak (around 12.7°) and the main perovskite peak (around 14.0°). The y-scale is the same for all four diffractograms.

transmission spectroscopy as a sharp edge rises around 500 nm for Ref-pvk[61] (Figure S6).

The origin of the perovskite degradation was investigated by GI-XRD.

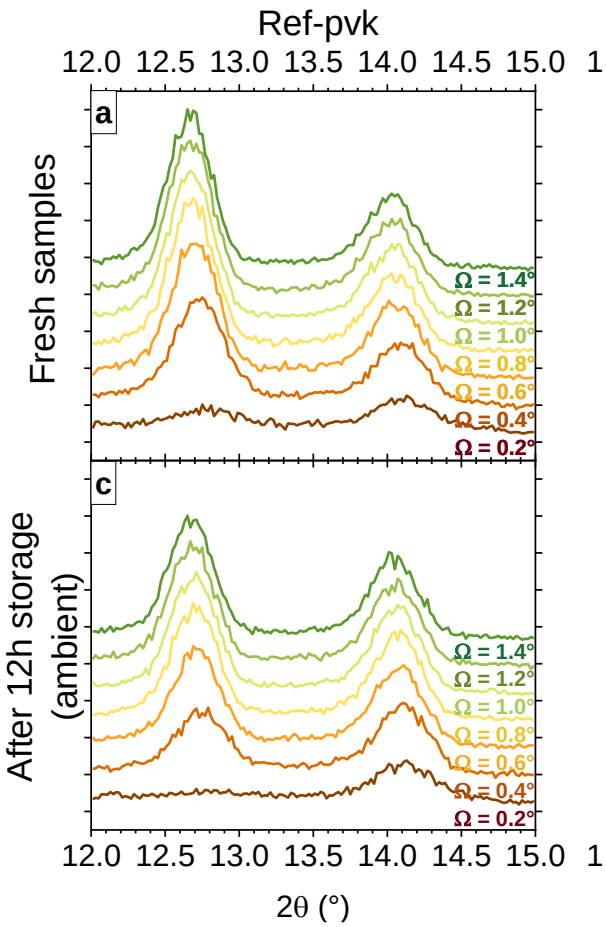

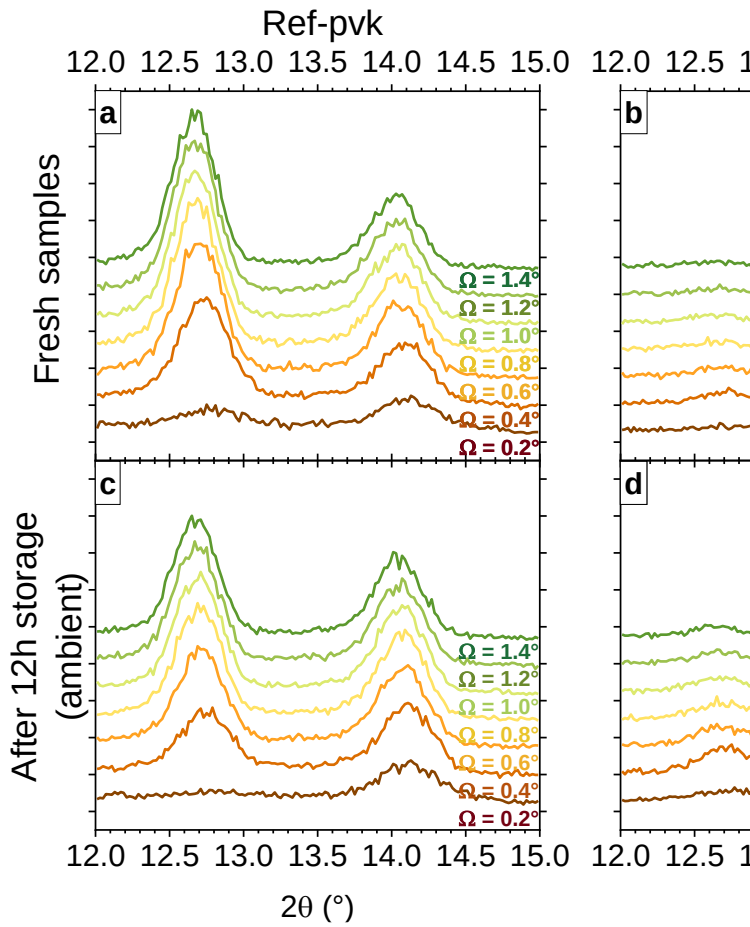

Figure 5 compares the diffractograms of Ref-pvk and AEPA-pvk with a grazing incidence angle going from $\Omega = 0.2°$ to 1.6° by step of 0.2°. Further information on the GI-XRD measurement procedure are given in the SI. The measurements have been performed right after the deposition of the perovskite to reduce atmospheric degradation (Figure 5.a, b). The angular window of interest has been set between $2\theta = 12°$ and $2\theta = 15°$, so that we can record the evolution of the main peak of interest (PbI_2, $2\theta = 12.7°$, and perovskite (110) plane, $2\theta = 14.1°$) within a short period of time (~30 min) and thus limit the impact of degradation during the measurements performed in ambient atmosphere.

As for AEPA-pvk, the pvk-peak is observed for $\Omega = 0.2°$, and its intensity increases up to $\Omega = 1.0°$, and then progressively decreases for larger angles. This is ascribed to the variations of the diffracting volume of the perovskite film which first increases with Ω, up to the point where the penetration length is about the thickness of the film. The diffracting volume of perovskite then decreases as Ω further increases. Note that at very low angles (around 0.2°), a signal loss can originate from X-ray reflection on the sample. The PbI_2-peak is very weak at any incidence angle, consistent with the XRD observations. Regarding Ref-pvk, the pvk-peak follows the same trend as for AEPA-pvk. This is contrasted by the remarkable evolution of the PbI_2-peak: its intensity increases up to $\Omega = 1.2°$, indicating that PbI_2 is located across the layer, down to the ZnO/perovskite interface. The same samples were investigated after storage for 12 hours in ambient air and light with the results shown in

	V_{oc} (mV)	J_{sc} (mA cm^{-2})	FF (%)	PCE (%)
Ref-pvk	*720*	*9,5*	*32,4*	*2,2*
AEPA-pvk	**1004**	*3,2*	*54,6*	*1,7*
FBzPA-pvk	*759*	**13,5**	**40,1**	**4,1**

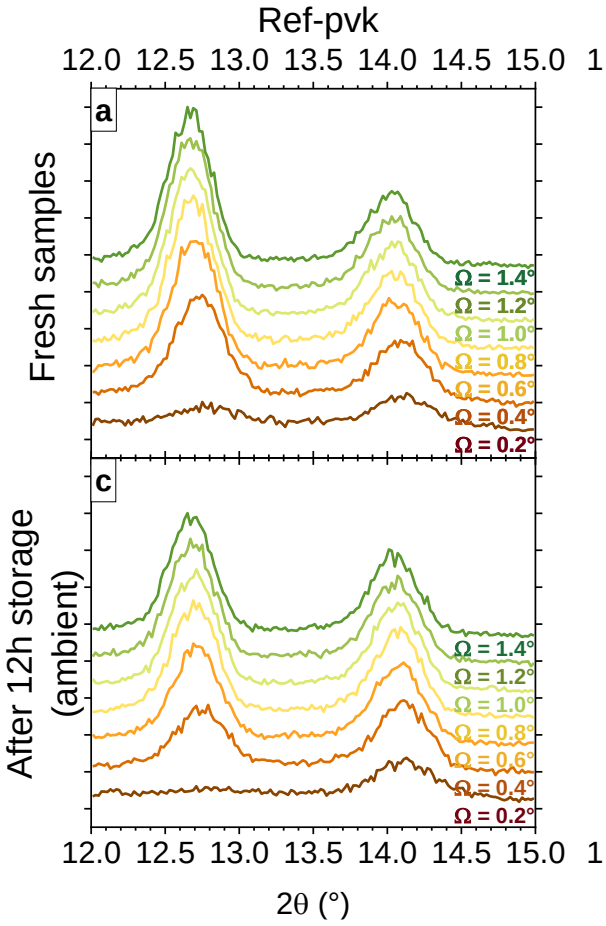

Figure 5.c and d. There are no obvious changes for Ref-pvk sample with the pvk-peak and PbI_2-peak reaching their maximum at Ω = 1.0° and Ω = 1.2° respectively. Regarding AEPA-pvk, a weak PbI_2-peak appears and reaches its maximum value at Ω = 0.4°.

Complete solar devices were prepared and characterized optoelectrically. The J-V parameters of the cells are presented in table 3, with the corresponding J-V characteristics displayed in Figure 6. Both Ref-pvk and FBzPA-pvk have a

Table 3: Photovoltaic parameters of the best performing cells made on Ref-pvk, AEPA-pvk and FBzPA-pvk substrates. The quantities are given for a reverse scan at 20 mV/s.

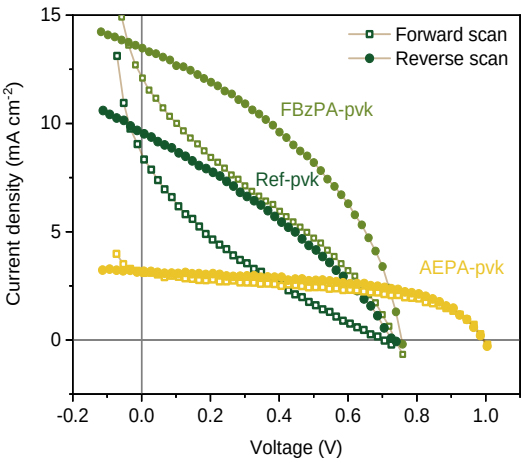

Figure 6: J-V characteristic of complete photovoltaic devices made on Ref-pvk, AEPA-pvk and FBzPA-pvk substrates under AM1.5G 1 sun simulated illumination

similar V_{OC} (720 mV and 749 mV respectively) but the modified sample shows a higher J_{sc} (9.5 mA·cm^{-2} vs. 13.5 mA·cm^{-2}, reverse scan). The two samples also exhibit a pronounced hysteresis between forward and reverse scan. On the other hand, the AEPA-pvk sample has a much higher V_{OC} of 1004 mV but a dramatically low J_{SC} of 3.2 mA·cm^{-2}, however with a lesser hysteresis. Overall, the best performing cell is the FBzPA-pvk with a power conversion efficiency (PCE) of 4.1% (reverse), stabilized at 2.4%. This shows a sensible increase as compared to the Ref-pvk which has a PCE of 2.2% (reverse) stabilized at 1.2%, comparable with efficiencies shown by Dong *et al.*[29].

DISCUSSION

Effective modification of the ZnO. ZnO layers deposited by ALD were modified with phosphonic acid derivatives composed of an anchor unit (-PO(OH)$_2$), a spacer (aryl, alkyl) and a functional group (-NH$_2$, -F) using a solution-processed method. Phosphonic groups are known to favor chemisorption of the molecule on metal oxides, and especially on ZnO surface[42], while the amine or fluorine terminations are aiming for a functionalization of the film. Surface characterization techniques including contact angle measurements, XPS and ATR-IR assessed the chemical modification of the ZnO film. The change of static contact angle and thus wettability of a surface is associated with a change of the energetics of the surface. This change can be induced by several factors such as an evolution of the surface morphology (for the same material, the wettability of a rough surface is less than that of a smooth one)[62] or a change in surface chemistry[63,64]. The change in hydrophilicity observed on the different samples is probably due to both effects. In the case of ZnO-ref immersed in EtOH:H$_2$O, SEM and XRD measurements (Figures S1, S2) strongly indicate a change in the nature and the morphology of the substrate. As for the modified ZnO substrates, contact angle measurements alone are not enough to confirm the effective coating of ZnO by the various molecules nor the way the molecules cover the surface, but rather indicate a difference in the surface energy between modified and reference ZnO.

Identification of the molecules on the surface. ATR-FTIR and XPS yield valuable information on the chemical environment of the different surfaces and confirm the proper deposition of 2-AEPA, 4-ABzPA and 4-FBzPA on the substrates.

It has been proposed in several studies that phosphonic acids chemisorb on zinc oxide via deprotonation of the acid and formation of one or several Zn-O-P bonds[41] (Figure S7) and the more bonds involved in the grafting, the stronger the interaction between the oxide and the molecule. Paniagua *et al.* reported non-resolved P 2p peaks around 133.4 eV for various phosphonic acids grafted on top of ITO, which was ascribed to phosphorus in PO_3^{2-} environment[65]. In the present work, the P $2p_{3/2}$ contribution is positioned at 134.2 eV for ZnO-AEPA and 133.7 eV for ZnO-ABzPA and ZnO-FBzPA, which is indicative of different protonated forms of the phosphonic acid group on the surface of modified ZnO. These observations are also supported by the P $2p_{3/2}$ position of the initial 4-FBzPA powder at 134.3 eV (Figure S8); for ZnO-ABzPA and ZnO-FBzPA a shift toward lower energies is observed. Keszthelyi *et al.* suggest that such a shift indicates a higher deprotonated state of the grafted molecule[66]. Deprotonation of the phosphonic acid is associated with a chemical interaction with the transition metal. On the contrary for ZnO-AEPA, the P 2p position does not vary much compared to that of the powder, which is in accordance with a deposition of a thicker multi-layer, as supported by AR-XPS data. This is thus indicative of different grafting processes between the linear and the aromatic molecules.

Two contributions for N 1s were observed, which are commonly ascribed to amine (-NH$_2$ around 400.0 eV) and ammonium groups (-NH$_3^+$ around 401.5 eV). In the case of n-(6-aminohexyl)aminopropyltrimethoxysilane grafted on TiO$_2$, Kassir *et al.* ascribed these contributions to physisorbed and chemisorbed species respectively[67], the physisorption involving a weak bonding between the protonated amine and a negatively-charged surface state of the oxide. These two contributions systematically appear in our samples. However, in light of the analysis of the P 2p line, we hypothesize that they originate from different phenomena. In ZnO-AEPA, the formation of a multilayer can explain the appearance of both protonation states, with the protonated amines

being involved in an ion-pairing interaction with the deprotonated phosphonic acid. In the case of ZnO-ABzPA, the P 2p signature indicates at least a partial grafting of the molecules on ZnO, and yet two contributions are found for N 1s. The ammonium groups could in this case arise from chemical bonding between the amine and the substrate[68]. AR-XPS also supports this hypothesis, in that it does not show any clear organization of the 4-ABzPA layer. In either of these cases, the layer grafted on ZnO does not resemble a well-organized monolayer. In the case of ZnO-FBzPA however, AR-XPS indicates that the 4-FBzPA molecules tend to have their phosphonic group anchored on the oxide, and their fluorine termination pointing away from the substrate, enabling a successful modification of the properties of the film. This orientation is also reinforced by the negligible modification of F 1s BE between the free molecule and ZnO-FBzPA (0.2 eV). It is hence proposed that in this case, the organization of the layer stems from the terminal function of the molecule used rather than from the spacer group. A sketch of the different molecule organizations on the surface is presented in SI (fig S10).

The nature of the grafted layer can also be deduced from the IR spectra. The mono-, bi- or tridentate nature of the bond between the phosphonic acids and ZnO should appear in the region of the P-O and P=O stretching modes. A first observation is that no contribution from P=O stretching modes can be brought forward in the 1200-1250 cm^{-1} range. The presence of such a contribution would have implied the presence of mono- or bi-dentate phosphonic acid moieties. A second observation is the prominent character of the contribution at ~1050 cm^{-1}, i.e., in the typical range where asymmetric ν(P-O) vibrations of PO_3 moieties are observed[69], suggesting a tridentate grafting to the surface. The contribution of symmetric ν(P-O) vibrations of PO_2 species can also contribute to this spectral range. However, for ZnO-FBzPA and ZnO-ABzPA, no corresponding contribution of asymmetric ν(P-O) vibrations of PO_2 species is observed above 1100 cm^{-1}, evidencing a tridentate configuration for the phosphonic group at the surface[70]. Notice that the vibrational bands at ~1050 cm^{-1} is somewhat broader for ZnO-ABzPA as compared to ZnO-FBzPA. This feature can be due to a small contribution of PO_2 species (associated to an unresolved contribution to the high-energy tail of the peak) and/or a structural disorder within the grafted layer, in agreement with XPS data. Conversely, the ZnO-FBzPA is also characterized by the weakness of the contribution at ~1000 cm^{-1}, clearly observed for ZnO-ABzPA and ZnO-AEPA; this contribution is often associated with unbound P-O(H) contributions. For ZnO-AEPA, two additional contributions are present at high energy, at ~1100 and ~1150 cm^{-1}. These contributions are tentatively assigned to symmetric ν(P-O) vibrations of PO_2 and C-N stretching vibrations[71], or admixtures of these modes. They are strong indications that on ZnO-AEPA, bidentate bonding of phosphonic groups coexist with tridentate bonding. The presence of bidentate bonding can be paralleled with the existence of a zwitterionic form suggested by the observation of a bending vibration band at ~1520 cm^{-1}. As a whole, tridentate bonding can be found for all molecules, at least as the major bonding configuration. This is in line with previous reports stating that phosphonic acids tend to form tridentate bonds with ZnO[34], and reported DFT calculations on ZnO-FBzPA that showed that tridentate configuration is more stable than the bidentate one[50].

Chemical passivation of the ZnO/perovskite interface. The poor chemical stability of the ZnO/perovskite interface has been widely reported and identified as one of the main reason for the lower performance of ZnO in perovskite solar cells in comparison to TiO_2[14]. Acid-base reactions between MA molecules and ZnO occur during the annealing of the perovskite, leading to the detrimental degradation into PbI_2. Accordingly in this study, the presence of pure PbI_2 in Ref-pvk has been evidenced by XRD and UV-vis spectroscopy.

This degradation mechanism can also be the cause of cavity formation in the perovskite layer and the inferior morphology of the surface observed in SEM for Ref-pvk. Similar morphologies of MA-containing perovskite have already been reported by Schutt *et al.*[25], and the replacement of MA by a mixture of FA and Cs led to improved morphologies. The change in the grains' compactness in our layers can be related to the degradation mechanism of the interface between MA and ZnO as suggested by Dkhissy *et al.*[72], which involves the decomposition of MAI into methylamine and HI, and reaction of HI with ZnO to form zinc-iodide species and water. Water does in turn further catalyze the decomposition of MAI, which leads to a rapid decomposition of the perovskite, as observed by XRD. A second degradation pathway could arise from the reaction between ZnO and ammonium (NH^{4+}) species. It has been shown that ZnO surface can be etched by the weak acid, leading to the formation of ammoniac and zinc salt[73,74]. On the other hand, none of these degradation-related features are observed in AEPA-pvk, which shows that the grafted layer of 2-AEPA chemically protects the interface between perovskite and ZnO.

This assertion is further confirmed by the GI-XRD study of the samples. Two degradation mechanisms are evidenced. First, a fast degradation occurring during the synthesis when

ZnO/perovskite are annealed above 80 °C as reported before[14]. This is characterized by a strong PbI_2 signal that increases with increasing scanning depth, hinting at the lead iodide being spread across the whole film. This feature is only seen for Ref-pvk. Second, a slower degradation process that is caused by ageing in atmospheric conditions. It has already been widely reported that moisture and oxygen are key extrinsic parameters of the perovskite degradation[75]. Here, this degradation is demonstrated by the lead iodide peak for AEPA-pvk, which did not exhibit any lead iodide phase observable in our XRD experiment right after the synthesis. Note that lead iodide peak reaches its maximum at quite low incidence angle, indicating the formation of lead iodide stemming rather from the air/perovskite interface than from the perovskite/ZnO interface at the back of the cell. The modification layer thus acts as a physical barrier between ZnO and perovskite, hence preventing the different reactants of the degradation mechanism from reacting with each other.

Finally, the results of the J-V analysis of the samples further support these conclusions. AEPA-pvk exhibits a V_{OC} above 1V, which is more in the range of average perovskite solar cells. A variation in open circuit voltage can be related to a change in the quality of the interfaces between the absorber and the extraction layers[76]. It has been shown previously on different oxide ETLs that using Lewis-bases (e.g. amine groups) or halogens can cure defects of the oxide as well as of the perovskite (undercoordinated iodide and lead specifically)[77,78]. In our case, we suspect that since 2-AEPA is forming a complete multilayer on the surface of ZnO, the interface between the absorber and the n-type extracting stack is indeed passivated allowing for a less defective interface, hence less non radiative recombinations and a higher open circuit voltage. On the other hand, the short-circuit current density is very low, in spite of a good morphology and a good absorption of the perovskite layer. Ab initio simulations show that the difference between the highest occupied molecular orbital (HOMO) and the lowest unoccupied molecular orbital (LUMO) of 2-AEPA is large (about 7 eV). We hypothesize that the insulator-like behavior of the multilayer is the reason impeding the extraction of the photogenerated carriers.

Regarding FBzPA-pvk, the J-V measurements combined with the SEM observations shed light on the covering of the grafted layer. The morphology resembles that of Ref-pvk, only with a smaller density of degraded spots. This suggests that the molecular layer does not completely cover ZnO, leaving places where the acid-base reaction can happen and degrade the perovskite. This translates on the J-V characteristics by a low V_{OC} similar to that of Ref-pvk probably caused by defect states related to this degradation process. The current density is however higher for the modified sample, in line with the fact that more photoactive material is preserved and can participate in the generation of photocarriers.

CONCLUSION

Functionalization of ZnO thin films with phosphonic acid derivatives can be an easy way to tune the properties of the film by modifying the architecture of the grafted molecule. In this work, we have demonstrated the effective grafting of an ALD-ZnO layer with three different molecules, having different spacers and functionalizing groups.

The grafted layers have been characterized by different surface characterization techniques (contact angle, XPS, FTIR). The results suggested that amine-terminated molecules tend to form hydrophilic multilayers, probably due to chemical interactions between the phosphonic and amine groups. On the other hand, fluorine-terminated molecules rather form a better-organized layer with an effective hydrophobic -F termination of the surface, which underlines the importance of the functional groups for the grating process.

The 2-AEPA and 4-FBzPA molecules were then integrated in a ZnO/halide perovskite interface, in order to probe its chemical passivation abilities. We show that the perovskite grows in more densely packed films on top of AEPA-modified ZnO compared to bare ZnO. Furthermore, the large contribution of the PbI_2 phase, which is known as an indicator of perovskite degradation leading to low performance in perovskite solar cells, was only observed when it is grown on bare-ZnO. This demonstrates the effective passivation of the interface by the grafted molecule, as a powerful method to preventing acid-base reaction between MA and ZnO and hence inhibit the degradation of the perovskite. 4-FBzPA shows however more mitigated improvements concerning the passivation of the interface, which was principally ascribed to a non-complete coverage of the ZnO substrate.

Even though the grating of molecules showed promising results, the integration in full devices lead to low efficiencies. Still the effects of the molecules and their assembly structure have been further reinforced by the J-V measurements.

We believe that these simple modifications opens up the way for exploring exciting opportunities where ALD-ZnO could not easily be used beforehand due to a lack of chemical passivation, by using more elaborate interfacial molecules.

EXPERIMENTAL

Device preparation

Substrates preparation. Two types of substrates were used depending on the stack which was studied. To study the grafting of the molecule on ZnO, n-type (100) Cz single side-polished silicon wafers with native oxide top layer (Neyco) were used. Si-substrates were ultrasonicated in RBS® detergent solution (2 vol%) for 5 minutes, rinsed with deionized water and dried under a flow of N_2. To study the ZnO/perovskite interface, 3 mm-thick fluorine-doped tin oxide (FTO) glass (Solems) was etched with zinc powder and HCl (0.1 M). These substrates were then ultrasonicated in RBS® detergent solution (2 vol%) for 30 minutes at 60 °C, rinsed with dionized water, then further ultrasonicated in acetone and propan-2-ol, and finally dried under a N_2 flow.

Deposition of ZnO by ALD. The substrates were transferred into a BENEQ TFS-200 ALD reactor for the deposition of 10 or 50 nm of zinc oxide. The deposition was performed according to a process described elsewhere[79].

Surface modification of ZnO. Fresh ZnO substrates were ultrasonicated in acetone and propan-2-ol for 10 minutes each. They were then cleaned with a UV-O_3 treatment, and directly transferred in the reaction vessel. 2-aminoethylphosphonic acid (2-AEPA), 4-aminobenzylphosphonic acid (4-ABzPA) or 4-fluorobenzylphosphonic acid (4-FBzPA) was dissolved in ethanol:H_2O 19:1 (50 mL) at 1 mM. For contact angle measurements, 4-FBzPA was dissolved in pure IPA. Control solutions consist in 50 mL of the sole solvents (ethanol:H_2O 19:1). After activation by UV-O_3, the samples were immersed and let in the solution under magnetic stirring, at room temperature for 10 min to 24 h. After deposition, the samples were thoroughly sonicated in IPA and dried under a flow of nitrogen.

Deposition of the perovskite layer. The samples were treated with UV-O_3 and transferred in the glovebox. A triple cation perovskite with precursor composition $Cs_{0.05}(MA_{0.17}FA_{0.83})_{0.95}Pb(I_{0.83}Br_{0.17})_3$ was deposited on top of the modified or unmodified ZnO layer, and the cells were completed by the addition of the according to a process described elsewhere[80].

Device characterization

X-ray photoelectron spectroscopy analysis (XPS)

XPS and AR-XPS analyses were carried out with a Thermo Electron K-Alpha+ spectrometer using a monochromatic Al-Kα X-Ray source (1486.6 eV). ARXPS experiments consist of tilting the considered sample from 0 to 60° (step of 10°) to perform non-destructive depth profiling by modifying the detection angle. The calibration of the spectrometer was performed according to Thermo Fisher procedure. The X-Ray spot size was 400 µm for a depth probed in the range of 10 nm. High energy resolution spectra were acquired using a Constant Analyzer Energy (CAE) mode of 10 eV and 0.05 eV as energy step size, without charge compensation for ZnO and ZnO-X samples but necessary for the 4-FBzPA powder. Data were processed using the Thermo Fisher scientific Avantage© data system.

X-ray diffraction analysis (XRD). XRD measurements are performed on a PanAnalytical Empyrean diffractometer with copper K-alpha radiation (λ=1.5406 Å) in Bragg-Brentano configuration. A dedicated modulus is added to carry out grazing incidence XRD measurements (GI-XRD), with incident beam angles ranging from 0.2° to 1.4°.

Scanning electron microscopy (SEM). SEM was used to observe the different layers with a Merlin VP Compact scanning electron microscope (SEM) provided by Zeiss.

Contact angle measurements. The wettability of the surfaces was assessed by contact angle measurements on a Krüss DSA 10 MK2 apparatus. Sessile drop method was used with 10 µL DI water droplets. For sake of reliability, each measurement was performed on at least three distinct samples every second for ten seconds and then averaged.

Attenuated total reflection Fourier transform infrared spectroscopy (ATR-FTIR). ATR-FTIR spectra were recorded using a Bomem MB100 FTIR spectrometer equipped with a liquid nitrogen-cooled MCT photovoltaic detector. The measurement chamber was purged with N_2 45 min prior to measurement. The Si prisms used as a substrate for the experiments were of typical size 15×14×0.5 mm^3, with a 45° angle, providing a number of ~14 useful reflections. The data were acquired with a 4 cm^{-1} resolution over 200 consecutive scans. The displayed spectra are plotted as absorbance (computed using the natural logarithm) and treated with an asymmetric least square smoother for the baseline subtraction as described elsewhere[81]. Note that ZnO-AEPA signal is overall more intense than for ZnO-ABzPA and ZnO-FBzPA, hence its multiplication by 0.1 to match the other samples' absorption range.

J-V characteristic. The current density–voltage (J–V) curves were measured with a solar simulator (Sol 3A class AAA) recorded using the commercial apparatus ARKEO. (*Cicci* Research) under illumination of 1 sun (100 mW cm^{-2}) AM 1.5G. The acquisition was performed at 20 mV/s after 5 minutes of light soaking at maximum powerpoint.

Acknowledgments

This project has been supported by the French Government in the frame of the program of investment for the future (Programme d'Investissement d'Avenir - ANR-IEED-002-01).
O.F. wishes to thank P. Baranek for the ab-initio calculations.

ASSOCIATED CONTENT

Supporting information. Diffractograms of ZnO-Ref and ZnO-AEPA after 10 min and 24 h immersion time (Figure S1). Micrographs of the associated surfaces (Figure S2). XPS survey spectra of ZnO-Ref, ZnO-AEPA, ZnO-ABzPA and ZnO-FBzPA (Figure S3). Associated high resolution XPS spectra of C1s region (Fig S4). List of identified BE for all samples (Table S1). Diffractograms of Ref-pvk and AEPA-pvk (Figure S5). Transmission spectrum of Ref-pvk and AEPA-pvk (Figure S6). Discussion on Ω-dependant GI-XRD measurements. Schematic representation of the different binding modes of phosphonic acids on a metal oxide layer (Figure S7). High resolution XPS spectra of 4-FBzPA powder (Figure S8).

AUTHOR INFORMATION

Corresponding author

* E-mail: olivier-o.fournier@edf.fr

Notes

The authors declare no competing financial interest.

REFERENCES

1. Wang, Z. L. Zinc oxide nanostructures: growth, properties and applications. *Journal of Physics: Condensed Matter* **16**, R829–R858 (2004).
2. Jayah, N. A. *et al.* High electron mobility and low carrier concentration of hydrothermally grown ZnO thin films on seeded a-plane sapphire at low temperature. *Nanoscale Res Lett* **10**, 7 (2015).
3. Ellmer, K., Klein, A. & Rech, B. *Transparent Conductive Zinc Oxide, Basics and Applications in Thin Film Solar Cells*. (2008).
4. Gupta, A., Kim, B. C., Edwards, E., Brantley, C. & Ruffin, P. Covalent functionalization of zinc oxide nanowires for high sensitivity p-nitrophenol detection in biological systems. *Materials Science and Engineering: B* **177**, 1583–1588 (2012).
5. Liao, Y., Hu, Z., Gu, Q. & Xue, C. Amine-Functionalized ZnO Nanosheets for Efficient CO2 Capture and Photoreduction. *Molecules* **20**, 18847–18855 (2015).
6. Jagadish, C. & Pearton, S. *Zinc Oxide Bulk, Thin Films and Nanostructures: Processing, properties and Applications*. (Elsevier Science, 2006).
7. Tsin, F. *et al.* Electrodeposition of ZnO window layer for an all-atmospheric fabrication process of chalcogenide solar cell. *Sci Rep* **5**, 8961 (2015).
8. Lange, I. *et al.* Zinc oxide modified with benzylphosphonic acids as transparent electrodes in regular and inverted organic solar cell structures. *Appl. Phys. Lett.* **106**, 113302 (2015).
9. Hadouchi, W., Rousset, J., Tondelier, D., Geffroy, B. & Bonnassieux, Y. Zinc oxide as a hole blocking layer for perovskite solar cells deposited in atmospheric conditions. *RSC Advances* **6**, 67715–67723 (2016).
10. Zhang, P. *et al.* Perovskite Solar Cells with ZnO Electron-Transporting Materials. *Advanced Materials* 1703737 (2017) doi:10.1002/adma.201703737.
11. Özgür, ü. *et al.* A comprehensive review of ZnO materials and devices. *Journal of Applied Physics* **98**, 041301 (2005).
12. He, S., Qiu, L., Ono, L. K. & Qi, Y. How far are we from attaining 10-year lifetime for metal halide perovskite solar cells? *Materials Science and Engineering: R: Reports* **140**, 100545 (2020).
13. Cho, A.-N. & Park, N.-G. Impact of Interfacial Layers in Perovskite Solar Cells. *ChemSusChem* **10**, 3687–3704 (2017).
14. Yang, J., Siempelkamp, B. D., Mosconi, E., De Angelis, F. & Kelly, T. L. Origin of the Thermal Instability in $CH_3NH_3PbI_3$ Thin Films Deposited on ZnO. *Chemistry of Materials* **27**, 4229–4236 (2015).
15. Schulz, P., Cahen, D. & Kahn, A. Halide Perovskites: Is It All about the Interfaces? *Chem. Rev.* **119**, 3349–3417 (2019).
16. Azmi, R. *et al.* High-Efficiency Low-Temperature ZnO Based Perovskite Solar Cells Based on Highly Polar, Nonwetting Self-Assembled Molecular Layers. *Adv. Energy Mater.* **8**, 1701683 (2018).
17. An, Q. *et al.* High performance planar perovskite solar cells by ZnO electron transport layer engineering. *Nano Energy* **39**, 400–408 (2017).
18. Zhang, D. *et al.* Surface Chlorination of ZnO for Perovskite Solar Cells with Enhanced Efficiency and Stability. *Sol. RRL* **3**, 1900154 (2019).
19. Tsarev, S. & Troshin, P. A. Surface modification of ZnO electron transport layer with thermally evaporated WO3 for stable perovskite solar cells. *Synthetic Metals* **269**, 116547 (2020).
20. Azmi, R., Lee, C.-L., Jung, I. H. & Jang, S.-Y. Simultaneous Improvement in Efficiency and Stability of Low-Temperature-Processed Perovskite Solar Cells by Interfacial Control. *Advanced Energy Materials* 1702934 (2018) doi:10.1002/aenm.201702934.
21. Cao, J. *et al.* Efficient, Hysteresis-Free, and Stable Perovskite Solar Cells with ZnO as Electron-Transport Layer: Effect of Surface Passivation. *Advanced Materials* 1705596 (2018) doi:10.1002/adma.201705596.
22. Chen, R. *et al.* High-Efficiency, Hysteresis-Less, UV-Stable Perovskite Solar Cells with Cascade ZnO–ZnS Electron Transport Layer. *Journal of the American Chemical Society* **141**, 541–547 (2019).
23. Tseng, Z.-L., Chiang, C.-H., Chang, S.-H. & Wu, C.-G. Surface engineering of ZnO electron transporting layer via Al doping for high efficiency planar perovskite solar cells. *Nano Energy* **28**, 311–318 (2016).
24. Song, J. *et al.* Highly efficient and stable low-temperature processed ZnO solar cells with triple cation perovskite absorber. *Journal of Materials Chemistry A* **5**, 13439–13447 (2017).
25. Schutt, K. *et al.* Overcoming Zinc Oxide Interface Instability with a Methylammonium-Free Perovskite for High-Performance Solar Cells. *Advanced Functional Materials* **29**, 1900466 (2019).
26. Zardetto, V. *et al.* Atomic layer deposition for perovskite solar cells: research status, opportunities and challenges. *Sustainable Energy & Fuels* **1**, 30–55 (2017).

27. Brinkmann, K. O., Gahlmann, T. & Riedl, T. Atomic Layer Deposition of Functional Layers in Planar Perovskite Solar Cells. *Sol. RRL* **4**, 1900332 (2020).

28. Park, H. H. Inorganic Materials by Atomic Layer Deposition for Perovskite Solar Cells. *Nanomaterials* **11**, 88 (2021).

29. Dong, X., Hu, H., Lin, B., Ding, J. & Yuan, N. The effect of ALD-Zno layers on the formation of $CH_3NH_3PbI_3$ with different perovskite precursors and sintering temperatures. *Chem. Commun.* **50**, 14405–14408 (2014).

30. Sandmann, A., Kompch, A., Mackert, V., Liebscher, C. H. & Winterer, M. Interaction of L -Cysteine with ZnO: Structure, Surface Chemistry, and Optical Properties. *Langmuir* **31**, 5701–5711 (2015).

31. Quiñones, R. *et al.* Study of Perfluorophosphonic Acid Surface Modifications on Zinc Oxide Nanoparticles. *Materials* **10**, 1363 (2017).

32. Sun, C. *et al.* Surface modification with EDTA molecule: A feasible method to enhance the adsorption property of ZnO. *Journal of Physics and Chemistry of Solids* **75**, 726–731 (2014).

33. Lange, I. *et al.* Tuning the Work Function of Polar Zinc Oxide Surfaces using Modified Phosphonic Acid Self-Assembled Monolayers. *Advanced Functional Materials* **24**, 7014–7024 (2014).

34. Hotchkiss, P. J., Malicki, M., Giordano, A. J., Armstrong, N. R. & Marder, S. R. Characterization of phosphonic acid binding to zinc oxide. *Journal of Materials Chemistry* **21**, 3107 (2011).

35. Lacher, S., Matsuo, Y. & Nakamura, E. Molecular and Supramolecular Control of the Work Function of an Inorganic Electrode with Self-Assembled Monolayer of Umbrella-Shaped Fullerene Derivatives. *J. Am. Chem. Soc.* **133**, 16997–17004 (2011).

36. Rongwei Zhang *et al.* Enhanced Electrical Properties of Anisotropic Conductive Adhesive With π-Conjugated Self-Assembled Molecular Wire Junctions. *IEEE Trans. Comp. Packag. Technol.* **32**, 677–683 (2009).

37. Jayalakshmi, G., Saravanan, K. & Balasubramanian, T. Impact of thiol and amine functionalization on photoluminescence properties of ZnO films. *Journal of Luminescence* **140**, 21–25 (2013).

38. Wallwork, M. L., Smith, D. A., Zhang, J., Kirkham, J. & Robinson, C. Complex Chemical Force Titration Behavior of Amine-Terminated Self-Assembled Monolayers. *Langmuir* **17**, 1126–1131 (2001).

39. Yang, L. *et al.* Effects of interface modification with self-assembled monolayers on the photovoltaic performance of CdS quantum dots sensitized solar cells. *Electrochimica Acta* **164**, 38–47 (2015).

40. Rupert, B. L., Mulvihill, M. J. & Arnold, J. Atom-Transfer Radical Polymerization on Zinc Oxide Nanowires. *Chem. Mater.* **18**, 5045–5051 (2006).

41. Smecca, E., Motta, A., Fragalà, M. E., Aleeva, Y. & Condorelli, G. G. Spectroscopic and Theoretical Study of the Grafting Modes of Phosphonic Acids on ZnO Nanorods. *J. Phys. Chem. C* **117**, 5364–5372 (2013).

42. Perkins, C. L. Molecular Anchors for Self-Assembled Monolayers on ZnO: A Direct Comparison of the Thiol and Phosphonic Acid Moieties. *The Journal of Physical Chemistry C* **113**, 18276–18286 (2009).

43. Gawalt, E. S., Avaltroni, M. J., Koch, N. & Schwartz, J. Self-Assembly and Bonding of Alkanephosphonic Acids on the Native Oxide Surface of Titanium. *Langmuir* **17**, 5736–5738 (2001).

44. Gao, W., Dickinson, L., Grozinger, C., Morin, F. G. & Reven, L. Self-Assembled Monolayers of Alkylphosphonic Acids on Metal Oxides. *Langmuir* **12**, 6429–6435 (1996).

45. Luschtinetz, R., Seifert, G., Jaehne, E. & Adler, H.-J. P. Infrared Spectra of Alkylphosphonic Acid Bound to Aluminium Surfaces. *Macromol. Symp.* **254**, 248–253 (2007).

46. Paniagua, S. A. *et al.* Phosphonic Acids for Interfacial Engineering of Transparent Conductive Oxides. *Chem. Rev.* **116**, 7117–7158 (2016).

47. Zhang, W. *et al.* Structure, stability and electrochromic properties of polyaniline film covalently bonded to indium tin oxide substrate. *Applied Surface Science* **367**, 542–551 (2016).

48. Norris, M. R. & Cossairt, B. M. CdSe on a mesoporous transparent conducting oxide scaffold as a photocathode. *J. Mater. Chem. A* **3**, 14585–14591 (2015).

49. Sharma, A., Hotchkiss, P. J., Marder, S. R. & Kippelen, B. Tailoring the work function of indium tin oxide electrodes in electrophosphorescent organic light-emitting diodes. *Journal of Applied Physics* **105**, 084507 (2009).

50. Wood, C., Li, H., Winget, P. & Brédas, J.-L. Binding Modes of Fluorinated Benzylphosphonic Acids on the Polar ZnO Surface and Impact on Work Function. *J. Phys. Chem. C* **116**, 19125–19133 (2012).

51. Knoops, H. C. M., Potts, S. E., Bol, A. A. & Kessels, W. M. M. Atomic Layer Deposition. in *Handbook of Crystal Growth* 1101–1134 (Elsevier, 2015). doi:10.1016/B978-0-444-63304-0.00027-5.

52. Ali, T. T. *et al.* Effect of pretreatment temperature on the photocatalytic activity of microwave irradiated porous nanocrystalline ZnO. *New J. Chem.* **39**, 321–332 (2015).

53. Gao, Z. & Banerjee, P. Review Article: Atomic layer deposition of doped ZnO films. *Journal of Vacuum Science & Technology A* **37**, 050802 (2019).

54. Béchu, S. *et al.* A challenge for x-ray photoelectron spectroscopy characterization of Cu(In,Ga)Se2 absorbers: The accurate quantification of Ga/(Ga + In) ratio. *Thin Solid Films* **669**, 425–429 (2019).

55. Longo, R. C., Cho, K., Schmidt, W. G., Chabal, Y. J. & Thissen, P. Monolayer Doping via Phosphonic Acid Grafting on Silicon: Microscopic Insight from Infrared Spectroscopy and Density Functional Theory Calculations. *Adv. Funct. Mater.* **23**, 3471–3477 (2013).

56. Knöfel, C., Martin, C., Hornebecq, V. & Llewellyn, P. L. Study of Carbon Dioxide Adsorption on Mesoporous Aminopropylsilane-Functionalized Silica and Titania Combining Microcalorimetry and in Situ Infrared Spectroscopy. *J. Phys. Chem. C* **113**, 21726–21734 (2009).

57. Lin-Vien, D., Colthup, N. B., Fateley, W. G. & Grasselli, J. G. Aromatic and Heteroaromatic Rings. in *The Handbook of Infrared and Raman Characteristic Frequencies of Organic Molecules* 277–306 (Elsevier, 1991). doi:10.1016/B978-0-08-057116-4.50023-7.

58. Saliba, M. *et al.* How to Make over 20% Efficient Perovskite Solar Cells in Regular (n–i–p) and Inverted (p–i–n) Architectures. *Chem. Mater.* **30**, 4193–4201 (2018).

59. Saliba, M. *et al.* Cesium-containing triple cation perovskite solar cells: improved stability, reproducibility and high efficiency. *Energy & Environmental Science* **9**, 1989–1997 (2016).

60. Jacobsson, T. J. *et al.* Unreacted PbI_2 as a Double-Edged Sword for Enhancing the Performance of

Perovskite Solar Cells. *J. Am. Chem. Soc.* **138**, 10331–10343 (2016).

61. Ferreira da Silva, A. *et al.* Optical determination of the direct bandgap energy of lead iodide crystals. *Appl. Phys. Lett.* **69**, 1930–1932 (1996).

62. Lee, M., Kwak, G. & Yong, K. Wettability Control of ZnO Nanoparticles for Universal Applications. *ACS Appl. Mater. Interfaces* **3**, 3350–3356 (2011).

63. Li, N. *et al.* Hydrophilic modification of polyvinylidene fluoride membranes by ZnO atomic layer deposition using nitrogen dioxide/diethylzinc functionalization. *Journal of Membrane Science* **514**, 241–249 (2016).

64. Hu, H., Ji, H.-F. & Sun, Y. The effect of oxygen vacancies on water wettability of a ZnO surface. *Phys. Chem. Chem. Phys.* **15**, 16557 (2013).

65. Paniagua, S. A. *et al.* Phosphonic Acid Modification of Indium–Tin Oxide Electrodes: Combined XPS/UPS/Contact Angle Studies. *J. Phys. Chem. C* **112**, 7809–7817 (2008).

66. Keszthelyi, T. *et al.* Investigation of Solid Surfaces Modified by Langmuir–Blodgett Monolayers Using Sum-Frequency Vibrational Spectroscopy and X-ray Photoelectron Spectroscopy. *J. Phys. Chem. B* **110**, 8701–8714 (2006).

67. Kassir, M. *et al.* Surface modification of TiO2 nanoparticles with AHAPS aminosilane: distinction between physisorption and chemisorption. *Adsorption* **19**, 1197–1209 (2013).

68. Hersh, L. S., Onyiriuka, E. C. & Hertl, W. Amine-reactive surface chemistry of zinc phosphate glasses. *J. Mater. Res.* **10**, 2120–2127 (1995).

69. Lin-Vien, D., Colthup, N. B., Fateley, W. G. & Grasselli, J. G. Organophosphorus Compounds. in *The Handbook of Infrared and Raman Characteristic Frequencies of Organic Molecules* 263–276 (Elsevier, 1991). doi:10.1016/B978-0-08-057116-4.50022-5.

70. Quiñones, R., Rodriguez, K. & Iuliucci, R. J. Investigation of phosphonic acid surface modifications on zinc oxide nanoparticles under ambient conditions. *Thin Solid Films* **565**, 155–164 (2014).

71. Lin-Vien, D., Colthup, N. B., Fateley, W. G. & Grasselli, J. G. Compounds Containing –NH2, –NHR, and –NR2 Groups. in *The Handbook of Infrared and Raman Characteristic Frequencies of Organic Molecules* 155–178 (Elsevier, 1991). doi:10.1016/B978-0-08-057116-4.50016-X.

72. Dkhissi, Y. *et al.* Stability Comparison of Perovskite Solar Cells Based on Zinc Oxide and Titania on Polymer Substrates. *ChemSusChem* **9**, 687–695 (2016).

73. Juarez-Perez, E. J., Ono, L. K., Uriarte, I., Cocinero, E. J. & Qi, Y. Degradation Mechanism and Relative Stability of Methylammonium Halide Based Perovskites Analyzed on the Basis of Acid–Base Theory. *ACS Appl. Mater. Interfaces* **11**, 12586–12593 (2019).

74. Kim, J.-K. & Lee, J.-M. Wet chemical etching of ZnO films using NH x -based (NH4)2CO3 and NH4OH alkaline solution. *J Mater Sci* **52**, 13054–13063 (2017).

75. Bisquert, J. & Juarez-Perez, E. J. The Causes of Degradation of Perovskite Solar Cells. *J. Phys. Chem. Lett.* **10**, 5889–5891 (2019).

76. Aydin, E., Bastiani, M. & Wolf, S. Defect and Contact Passivation for Perovskite Solar Cells. *Adv. Mater.* 1900428 (2019) doi:10.1002/adma.201900428.

77. Shallcross, R. C., Olthof, S., Meerholz, K. & Armstrong, N. R. Impact of Titanium Dioxide Surface Defects on the Interfacial Composition and Energetics of Evaporated Perovskite Active Layers. *ACS Appl. Mater. Interfaces* **11**, 32500–32508 (2019).

78. Wang, F., Bai, S., Tress, W., Hagfeldt, A. & Gao, F. Defects engineering for high-performance perovskite solar cells. *npj Flex Electron* **2**, 22 (2018).

79. Le Tulzo, H., Schneider, N., Lincot, D. & Donsanti, F. Toward an all-Atomic Layer Deposition (ALD) process for Cu(In,Ga)(S,Se)2 (CIGS)-type solar cell. *Solar Energy Materials and Solar Cells* **200**, 109965 (2019).

80. Ramos, F. J. *et al.* Versatile Perovskite Solar Cell Encapsulation by Low-Temperature ALD-Al2O3 with Long-Term Stability Improvement. *Sustainable Energy* 13.

81. Eilers, P. H. C. A Perfect Smoother. *Anal. Chem.* **75**, 3631–3636 (2003).